Large Valley Splitting in van der Waals Heterostructures with Type-III Band Alignment

Qianze Li, Ke-Qiu Chen, and Li-Ming Tang*

Department of Applied Physics, School of Physics and Electronics, Hunan University, Changsha 410082, China

(Received 27 March 2019; revised manuscript received 15 December 2019; published 30 January 2020)

Lifting the valley degeneracy of monolayer transition-metal dichalcogenides (TMDs) can substantially break the balance of carriers in the K and K' valleys. This opens a promising way to utilize magnetic materials to break time-reversal symmetry to achieve valley splitting. In the work presented in this paper, we find that the magnitude of the valley splitting in TMD-based van der Waals (vdW) heterostructures is correlated with the strength of the magnetic proximity effect, which is positively related to the interlayer charge transfer and Coulomb interaction. As a result, for the same stacking, large valley splittings can be obtained only when the vdW heterostructure has a type-III, instead of a type-I or type-II, band alignment. We demonstrate this finding in TMD/NiY_2 ($Y = \mathrm{Cl, Br, I}$) vdW heterostructures in detail based on first-principles calculations, and predict several heterostructures with large valley splittings. This discovery can help to distinguish whether a magnetic material can enable TMDs to produce large valley splittings, and guide experiments for technological applications.

DOI: 10.1103/PhysRevApplied.13.014064

I. INTRODUCTION

Utilizing and manipulating the valley degree of freedom of electrons as an information carrier has attracted increasing interest [1–3]. The combination of a large spin-orbit coupling (SOC) and the locked degrees of freedom between the spins and valleys makes monolayer transition-metal dichalcogenides (TMDs) the best candidate materials for studies of valleytronics [2,4,5]. Because of time-reversal symmetry (TRS) protection, the intrinsic pure spin-valley Hall current between the two inequivalent K and K' valleys with degenerate energies is not available [6,7], but such a current can be achieved by means of optical [8–12], electric [13,14], and magnetic modulation [15–25]. Among these methods, breaking TRS through magnetism is the most effective method to lift the valley degeneracy and achieve a polarized spin-valley current.

Generally, there are three schemes to use magnetic effects to break TRS in TMDs. The first is to use an external magnetic field directly [15,16], the second is to use doping to generate an intrinsic magnetic moment in the TMD [17–19], and the last is to create heterostructures on magnetic substrates to create a magnetic proximity effect [20–25]. However, the desired valley splitting has not largely been obtained by the first scheme; only a splitting efficiency as low as 0.1–0.2 meV/T has been obtained when an external magnetic field was utilized directly [15,16]. Although it has been demonstrated that both p-type and n-type doping can induce an intrinsic magnetic moment in TMDs and produce large valley splittings [17–19], the stability of the doped system and band scattering from the impurities will damage its application as a valley electronic device. In the last scheme, the magnetic substrate must have an effective magnetic moment in the vertical direction, since the spin quantization axis of TMDs is out-of-plane. Recently, large valley splittings have been achieved both theoretically and experimentally in two-dimensional (2D) TMD/bulk (three-dimensional, 3D) magnetic-substrate heterostructures [20–23,26]. For example, in TMD/EuO(EuS), a giant splitting of over 44 meV was predicted in monolayer $MoTe_2$ by first-principle calculations [20,21]. The enhancement of valley splitting was also confirmed in experiments, where the splitting efficiency was one to two orders of magnitude larger than that caused by external magnetic fields, and reached 2.5 meV/T [22] and 16 meV/T [26], respectively. The magnitude of the valley splitting in such 2D/3D heterostructures formed from monolayer TMDs and bulk magnetic materials is indeed significantly increased, but defects in the form of lattice mismatches, polycrystalline anisotropic magnets, and dangling bonds at the interface will limit their application to devices [24].

With the development of thin-film-preparation technology and high-throughput calculations, an increasing number of 2D magnetic semiconductor materials have been discovered [27,28]. It seems that the dilemmas associated with 2D/3D heterostructures may be avoided by using van der Waals (vdW) heterostructures with a 2D/2D structure [29,30]. Recently, a variety of magnetic substrates, such as

*lmtang@semi.ac.cn

the layered ferromagnetic semiconductor CrI_3, have been tried to induce valley splitting in TMDs [24,31,32], and a modest splitting of about 3.5 meV, which corresponds to an effective magnetic exchange field of 13 T, was observed [24]. Despite this, satisfactory magnetic substrates for the purpose of achieving a large valley splitting are few and far between. What is more frustrating is that it is still not clear what kind of magnetic substrate should be selected and what types of heterostructures are required to produce a large valley splitting. Therefore, finding a rule for the realization of valley splitting in TMDs in heterostructures has become important. In heterojunction physics, heterostructures are classified into three types, namely type I, type II, and type III [33]. Specifically, when semiconducting materials A and B are merged, if the valence-band maximum (VBM) and conduction-band minimum (CBM) satisfy the relation $VBM_A < VBM_B < CBM_B < CBM_A$, the resulting heterostructure is type I; if $VBM_A < VBM_B < CBM_A < CBM_B$, it is type II; and if $VBM_A < CBM_A < VBM_B < CBM_B$, it is type III. The type-I and II heterostructures are still semiconductors, while the type-III heterostructures become metals. The stronger charge transfer in type-III heterostructures enhances the magnetic proximity effect and the Coulomb interaction between the substrate and the TMD to possibly enhance the valley splitting. This implies opportunities to find large valley splittings in type-III vdW heterostructures.

In this paper, we perform a comparative study of valley splitting in a series of 2D/2D vdW heterostructures and find that only type-III, rather than type-I and type-II, band-alignment heterostructures can provide large valley splittings. Our research on stacking also shows that, for the same stacking, type-III heterostructures have the largest valley splitting compared with type-I and type-II ones. We demonstrate this criterion with TMD/NiY_2 vdW heterostructure models in detail, and predict several vdW heterostructures with large valley splittings.

II. COMPUTATIONAL METHODS

First-principles calculations are performed using the Vienna *ab initio* simulation package (VASP) [34]. We approximate the exchange-correlation potential with the Perdew-Burke-Ernzerhof (PBE) functional [35]. Projector-augmented-wave potentials are used [36]. The tetrahedron method is used for structural optimization and for total-energy calculations. All of the atoms are optimized until the total energy converges to below 10^{-5} eV, and the forces acting on the atoms are less than 10^{-2} eV/Å. The plane-wave energy cutoff is set to 500 eV, and the Monkhorst-Pack grid of the k-point mesh is set to $11 \times 11 \times 1$. To avoid interactions between periodic images, the thickness of the vacuum regions is not smaller than 16 Å. Spin-orbit coupling and van der Waals interactions are taken into account to optimize the heterostructure geometry, as well as to perform further calculations by the DFT-D2 method [37]. To consider the on-site Coulomb interaction in NiY_2, the GGA+U calculation method is adopted [38,39], and the Coulomb and exchange parameters U and J are set to 4.0 and 0.8 eV, respectively, for the d orbitals of the Ni atom [40]. For the calculation of the Berry curvature, we employ the maximally localized Wannier-function method as implemented in the WANNIER90 package [41,42]. Ten d orbitals of the Mo atom and six p orbitals of each Te atom are selected as the initial orbital projections, and a $16 \times 16 \times 1$ uniform k grid is used for the construction of the maximally localized Wannier function. The difference in the spread of the total Wannier functions between two successive iterations converges to 10^{-10} Å ^{2} within 2000 iterative steps.

III. RESULTS AND DISCUSSION

A. Geometry, band alignment, band structure, and Berry curvature

The transition-metal dihalides NiY_2 (Y = Cl, Br, I) crystallize in a CdI_2-type structure, where edge-sharing NiY_6 octahedra form two-dimensional triangular lattice sheets, stacked along the z direction with weak van der Waals interactions between them. The crystal structure of monolayers of these compounds is the same as that of the 1T phase of monolayer TMDs [43]. The optimized in-plane lattice constants of the monolayer structures are 3.48, 3.68, and 3.95 Å, respectively, as Y varies from Cl to I, whereas the lattice constants for TX_2 monolayers (T = Mo, W; X = S, Se, Te) are 3.16, 3.35, and 3.56 Å, respectively, as X varies from S to Te. To reduce the lattice mismatch to less than 5%, $MoSe_2/NiCl_2$, $WSe_2/NiCl_2$, $MoTe_2/NiCl_2$, $WTe_2/NiCl_2$, $MoTe_2/NiBr_2$, and $WTe_2/NiBr_2$ heterobilayers are created with corresponding 1×1 unit cells, and the other TX_2/NiY_2 heterobilayers are constructed by use of superlattice structures with slabs of monolayer TX_2 (2×2) on top of NiY_2($\sqrt{3} \times \sqrt{3}$).

Three pairs of typical stackings, containing a total of six different stable stacking configurations, are considered for comparison. To show these stacking configurations more clearly, we choose a lattice-matched $WTe_2/NiCl_2$ heterobilayer in the form of a 3×3 superlattice pattern as an example, as shown in Fig. 1(a). The specific features of the six configurations, denoted by (C-1/C-1′), (C-2/C-2′), and (C-3/C-3′), are as follows. The configuration in which an interfacial Te1 atom is directly above a Ni atom (Te1⊥Ni) and a W atom is directly above an interfacial Cl1 atom (W⊥Cl1), indicated as (Te1⊥Ni & W⊥Cl1), is C-1; the configuration in which an interfacial Te1 atom is directly above a Ni atom but a W atom is directly above a noninterfacial Cl2 atom, expressed as (Te1⊥Ni

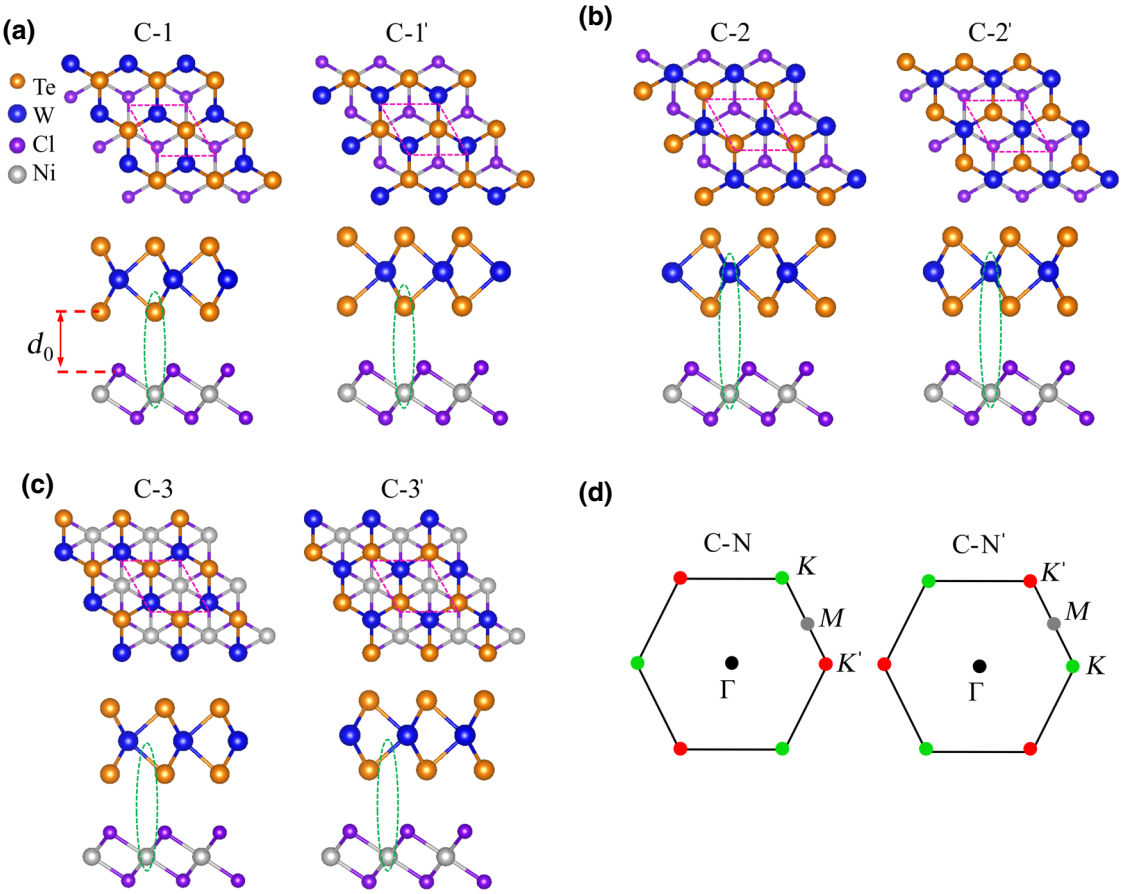

FIG. 1. Top and side views of $WTe_2/NiCl_2$ heterostructure in six stackings. (a) The C-1 and C-1′ stackings have a Ni atom directly on top of an interfacial Te atom. (b) The C-2 and C-2′ stackings have a Ni atom directly on top of a W atom. (c) The C-3 and C-3′ stackings have no atom superpositions with Ni atoms. The pink dashed line indicates the unit cell of the heterobilayer. d_0 is the interlayer distance. (d) First Brillouin zone of monolayer TMDs; the high-symmetry point K for C-N stackings (left) corresponds to the K' point for C-N′ stackings (right).

& W⊥Cl2), is C-1′. In the same way, the (W⊥Ni & Te1⊥Cl2) configuration is C-2, the (W⊥Ni & Te1⊥Cl1) configuration is C-2′, the (Te1⊥Cl1 & W⊥Cl2) configuration is C-3, and the (Te1⊥Cl2 & W⊥Cl1) configuration is C-3′. Accordingly, (C-1/C-1′) has a superposition of Ni and Te atoms, (C-2/C-2′) has a superposition of Ni and W atoms, and (C-3/C-3′) has no superposition of Ni and W or Te atoms. In fact, C-1′ and C-2′ (C-3′) can be seen as 60° (180°) counterclockwise rotations of C-1 and C-2 (C-3) while keeping the NiY_2 layer stationary. So, for a monolayer of WTe_2, the high-symmetry point K in the Brillouin zone for the C-N stacking is the K' point for the C-N′ stacking.

NiY_2 can be exfoliated as a stable monolayer structure [28], having a similar crystal structure to TMDs [43], and possessing ferromagnetism with a high Curie temperature [44] and an intrinsic band gap from 0.88 to 2.22 eV (calculated from GGA + SOC + U, with $U = 4$ eV). This means that these structures not only are excellent magnetic substrates for experiments, but also allow us to obtain structurally stable TMD/NiY_2 vdW heterostructures with all band-alignment types to investigate the mechanisms of valley splitting achieved in heterostructures. As shown in Fig. 2(a), the MoS_2/NiI_2 and WS_2/NiI_2 heterostructures show type-I band alignment, $WTe_2/NiCl_2$, $WTe_2/NiBr_2$, and WTe_2/NiI_2 show type-III band alignment, and the other heterostructures show type-II band alignment [33]. Note that the band gap of the monolayer TMDs is obtained with the PBE functional, because this is agrees well with the reported experimental value. Taking MoS_2 as an example, the gap of 1.72 eV obtained with the PBE functional is close to the reported experimental value of 1.80 eV [45]. The feasibility and thermal stability of these heterostructures are determined by the binding energy and the phonon spectrum [46–49], respectively. The results and the electronic band structures are presented in Figs. S1 and S2 in the Supplemental Material [50]). In the following example, a $WTe_2/NiCl_2$ heterobilayer is used to illustrate the band-structure characteristics of these vdW heterostructures.

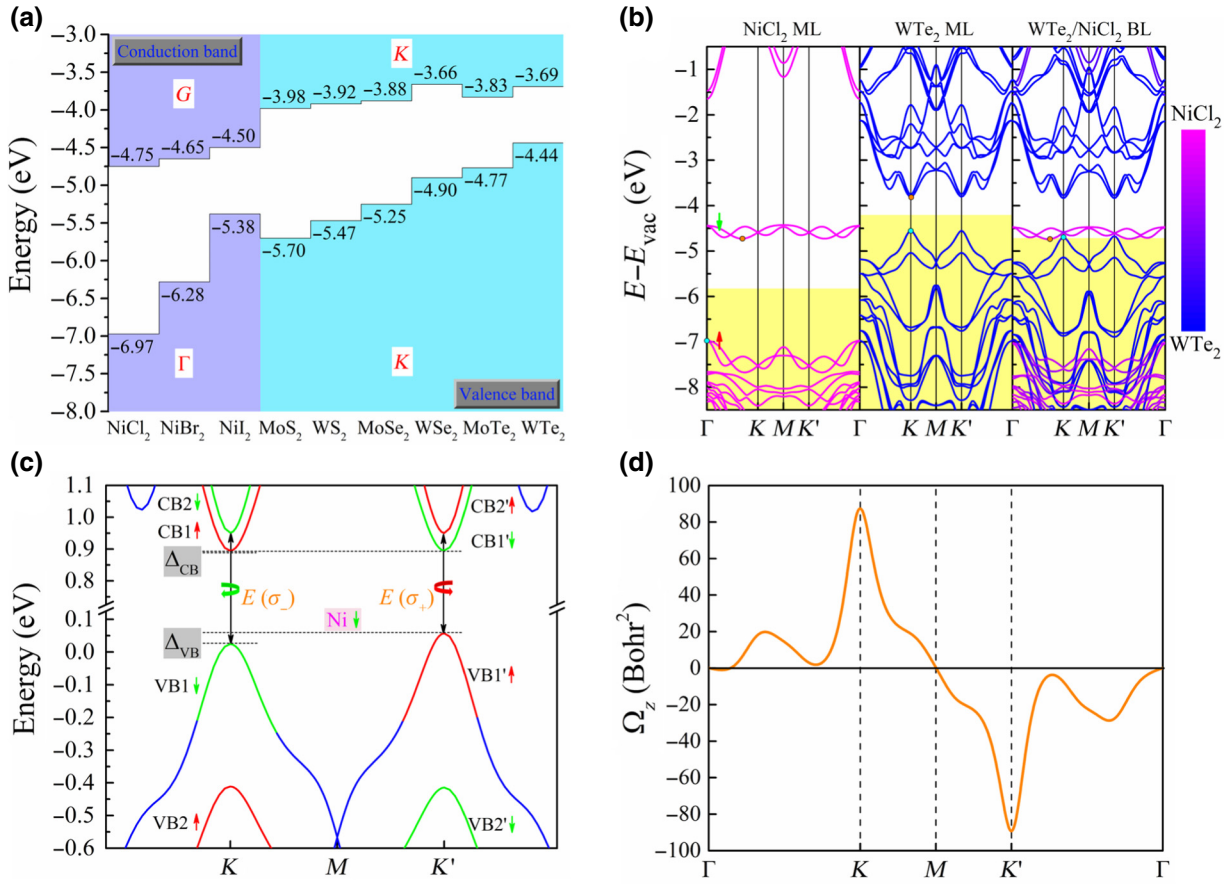

FIG. 2. (a) Band alignment of monolayer NiY_2 and TMDs. The vacuum level is taken as the zero reference. (b) Band structure of $NiCl_2$ monolayer, WTe_2 monolayer, and $WTe_2/NiCl_2$ heterobilayer. The green and red arrows denote the spin-down and spin-up bands, respectively, for monolayer $NiCl_2$. E_{vac} denotes the vacuum energy, and the Fermi level lies at the intersection of the white and yellow regions. (c) Enlarged details of the valley splitting and optical selection rule for the WTe_2 monolayer in the $WTe_2/NiCl_2$ heterostructure. Δ_{VB} and Δ_{CB} are the valence- and conduction-band valley splittings, respectively. $E(\sigma_\pm)$ indicates the energy of photons with circular polarizations $\sigma_\pm$. (d) Calculated Berry curvature Ω of the monolayer WTe_2 in the heterobilayer at the high-symmetry k-points.

Figure 2(b) presents the band structure of a $NiCl_2$ monolayer (ML), a WTe_2 monolayer, and a C-2-stacked $WTe_2/NiCl_2$ bilayer (BL). It is found that the band edges of monolayer $NiCl_2$ are composed of 3d states of Ni, and the VBM is spin-up but the CBM and CBM+1 are spin-down, exhibiting ferromagnetic semiconducting properties. The magnetic moments of the Ni and Cl atoms are 1.72 and 0.11 μ_B, respectively. When the vacuum-level alignment is adopted, it is obvious that the VBM (Γ point) is much lower than that of WTe_2, and the CBM (between Γ and K) is also slightly smaller than the VBM of WTe_2. These band-edge characteristics make the spin-polarized empty states of $NiCl_2$ mix with the pseudospin valley located at the VBM of WTe_2 in the $WTe_2/NiCl_2$ heterobilayer, thus forming a type-III heterostructure. Because of the large energy difference between CBM+1 and CBM+2 in $NiCl_2$, the conduction-band edges of the WTe_2 are not hybridized. This means that the composition of the heterostructure does not change the energy valley at the conduction-band edge of WTe_2.

Figure 2(c) presents enlarged details of the band edges of WTe_2, which are separated from the heterobilayer band; the energy bands from Ni d states with a spin-down state are not shown. The splitting Δ_{VB}/Δ_{CB} between the valence- and conduction-band valleys is the energy difference between the two valley extrema of the WTe_2 [20], i.e., $\Delta_{val}^{VB/CB} = E_{K'}^{VB/CB} - E_{K}^{VB/CB}$. As shown in Fig. 2(c), valley splitting is indeed achieved in the K and K' valleys, and Δ_{VB} and Δ_{CB} reach values of 33.1 and 0.6 meV, respectively. So, the total K–K' valley splitting, which is derived as $\Delta_{KK'} = \Delta_{VB} - \Delta_{CB}$, is 32.5 meV. The realization of valley splitting also gives rise to a difference in the energies of the circularly polarized optical transitions, where $\Delta_{opt}^{+} = E_{K(\uparrow)}^{CB2,+} - E_{K(\uparrow)}^{VB1,+} = 893.1$ meV for right-handed polarized light σ_+, and $\Delta_{opt}^{-} = E_{K'(\downarrow)}^{CB2,-} - E_{K'(\downarrow)}^{VB1,-} = 926.9$ meV for left-handed polarized light σ_-. Thus the difference in optical-transition energies between the two polarizations of the light, i.e., $E(\sigma_+) - E(\sigma_-)$, reaches a substantial value of 33.8 meV, which is also nearly the value of

the total valley splitting $\Delta_{KK'}$. Considering the measured Zeeman valley-splitting rate of approximately 0.2 meV/T in monolayer TMDs for external magnetic fields, this corresponds to the splitting produced by a 163 T magnetic field. Note that the size of the splitting achieved in the $WTe_2/NiCl_2$ heterobilayer is an order of magnitude larger than in the case of a WSe_2/CrI_3 heterobilayer [24,31,32], and even close to the substantial splitting obtained in a $MoTe_2$/EuO heterostructure [20,21]. This will allow valley selection to work within a rather wide spectral range: as long as the photon energy of the polarized light used satisfies $\Delta_{\text{opt}}^{+} < \hbar\omega < \Delta_{\text{opt}}^{-}$, valley-dependent electron-hole pairs can be generated only in the K' valley. Although the Fermi level crosses these two valleys in WTe_2 in a type-III $WTe_2/NiCl_2$ heterobilayer, the valleys can be shifted below the Fermi level by means of gate-voltage regulation and vertical-stress regulation [51], and so electron-hole pairs between the two valleys could be still generated by circularly polarized light. And, interestingly, a total valley splitting of about 14.8 meV is achieved in a type-II $MoTe_2/NiCl_2$ bilayer at the equilibrium distance, and so electron-hole pairs can be obtained by the use of circularly polarized light directly. Additionally, it is further clarified in Fig. 2(d) that after the introduction of the magnetic substrate, it is precisely because of the magnetic proximity effect that TRS is broken in the WTe_2, resulting in a valley polarization. The Berry curvature takes opposite signs near the K and K' valleys, with unequal values, revealing that the spin-valley characteristics of WTe_2 are still well preserved and that spin-valley splitting is realized [52]. Therefore, NiY_2 could be a new class of excellent 2D layered magnetic substrates for TMDs.

B. Effects of stacking on valley splitting

It is well known that the stacking of a heterostructure affects the electronic properties. To study the effects of stacking on valley splitting, the lattice-matched type-II $MoTe_2/NiCl_2$ and type-III $WTe_2/NiCl_2$ heterobilayers are selected for comparison. We list the six stable stackings, the distances $d_{T\text{-Ni}}$, $d_{\text{Te-Ni}}$, $d_{T\text{-Cl}}$, and $d_{\text{Te-Cl}}$ (where T represents a transition-metal atom, i.e., Mo or W), the equilibrium interlayer distance d_0, and the size of the valley splitting in Table I. Clearly, for the two heterobilayers, the C-2 stacking has the largest valley splitting, and this splitting is close to that for the C-1 and C-1′ stackings, but significantly larger than that for the other three stackings. As the variation of the size of the valley splittings in the two types of heterostructure is completely consistent for these six stackings, we may use the $WTe_2/NiCl_2$ heterobilayer as an example to investigate the effects of the stacking on the splitting.

As listed in Table I, after full relaxation, the value of $d_{\text{Te-Cl}}$ is the same in all of the stacking configurations, and the C-2′ and C-3 stackings have the same interlayer spacing d_0, which is larger than that for the other four stackings. We can see that the size of the splitting is closely related to the interlayer spacing d_0, and the smaller the value of d_0, the larger the valley splitting, except for the case of the C-3′ stacking. This is because the K and K' valleys of WTe_2 are mostly composed of 5d states of W atoms and a small amount of p (and s) states of Te atoms, which can cause couplings to occur with the 3d states of Ni atoms that affect the splitting. It can be seen from the results for C-1 and C-1′ and for C-2 and C-2′ that the valley splitting has no connection with $d_{\text{W-Cl}}$ and $d_{\text{Te-Cl}}$, but is closely related to $d_{\text{W-Ni}}$ and $d_{\text{Te-Ni}}$, and the smaller the values of $d_{\text{W-Ni}}$ and $d_{\text{Te-Ni}}$, the larger the splitting. Namely, the effect of coupling between W and Cl atoms on the size of the splitting can be neglected (because there are nearly no s,p states of Cl atoms at the band edges at K and K'), but the coupling between W and Ni atoms and between Te and Ni atoms is the dominant factor in achieving a relatively large splitting

TABLE I. Comparison between type-II and type-III heterostructures for six stackings. d_0 is the equilibrium interlayer distance, and $d_{M\text{-}N}$ is the shortest distance between the M and N atoms. T represents a Mo (W) atom in monolayer Mo(W)Te_2. Δ_{VB}, Δ_{CB}, and $\Delta_{KK'}$ are the valence-band, conduction-band, and total valley splittings, respectively.

Type	Stacking	$d_{T\text{-Ni}}$ (Å)	$d_{\text{Te-Ni}}$ (Å)	$d_{T\text{-Cl}}$ (Å)	$d_{\text{Te-Cl}}$ (Å)	d_0 (Å)	Δ_{VB} (meV)	Δ_{CB} (meV)	$\Delta_{KK'}$ (meV)
Type II	C-1	6.72	4.57	6.17	3.82	3.24	9.5	−3.5	13
	C-1′	6.72	5.59	6.50	3.83	3.26	−9.4	4.0	−13.4
	C-2	6.42	5.02	5.47	3.84	3.26	11.3	−3.5	14.8
	C-2′	6.99	5.54	6.01	3.83	3.83	−1.4	1.2	−2.6
	C-3	7.27	5.54	6.95	3.83	3.83	−1.1	−1.2	0.1
	C-3′	6.72	5.00	6.17	3.83	3.24	2.7	3.9	−1.2
Type III	C-1	6.67	4.53	6.13	3.78	3.21	28.1	1	27.1
	C-1′	6.72	4.57	5.46	3.82	3.24	−25.8	−0.9	−24.9
	C-2	6.37	4.98	5.44	3.81	3.22	33.1	0.6	32.5
	C-2′	6.92	5.49	5.96	3.77	3.77	−6.7	−0.4	−6.3
	C-3	7.21	5.48	5.95	3.77	3.77	−1	0.8	−1.8
	C-3′	6.70	4.99	5.06	3.82	3.24	2.3	−2.5	4.8

in the heterobilayer. This is verified by the case of the C-3′ and C-3 stackings, where there is no atom superposition of the form (W⊥Ni) or (Te⊥Ni) in these two stackings, and then the coupling between W and Ni atoms and between Te and Ni atoms is weakest, leading to a sharp decrease in the splitting. Even if the C-3′ stacking has the same values of $d_{\text{W-Ni}}$ and the interlayer spacing d_0 as those for the C-1 and C-1′ stackings, the valley splitting is still an order of magnitude smaller than that for the C-1 and C-1′ stackings. Therefore, the adjustment of the valley splitting by the stacking actually occurs by regulation of the strength of the magnetic coupling effect, which is mainly related to the interatomic distance and the atom superposition of W or Mo and Ni. Interestingly, a similar situation was also found in type-II CrI_3/WSe_2 vdW heterostructures by Zhang and coworkers [32].

Moreover, we can also see that for the same stacking, the size of the valley splitting in the type-III $WTe_2/NiCl_2$ bilayer is always larger than that in the type-II $MoTe_2/NiCl_2$ bilayer. As the C-N (C-N′) stacking has a phase difference of 60° (180°), the K (K') high-symmetry point for the C-N stacking corresponds to K' (K) for the C-N′ stacking of the monolayer TMDs. When the same Brillouin-zone path $\Gamma KMK'\Gamma$ is used to calculate the electronic energy band, where Γ is (0,0,0), K is $(-\frac{1}{3},\frac{2}{3},0)$, M is $(0,\frac{1}{2},0)$, and K' is $(\frac{1}{3},\frac{1}{3},0)$, Δ_{VB} and Δ_{CB} for the C-N stacking have values opposite to those for the C-N′ stacking, as shown in Table I. The energy of the VBM of the TMDs near the K valley which has the same spin state (spin-down) as the NiY_2 is also always smaller than that for the K' valley. These phenomena indicate that charge transfer and Coulomb interaction are the key factors that affect the size of the valley splitting.

C. Effects of charger transfer on valley splitting

In Figs. 3(a)–3(c), we present the calculated interfacial charge transfer and charge redistribution in the type-I MoS_2/NiI_2 bilayer, the type-II $MoTe_2/NiBr_2$ bilayer, and the type-III $WTe_2/NiCl_2$ bilayer. The charge-density difference ($\Delta\rho$) is calculated from

$$\Delta\rho = \Delta\rho_{(\text{TMD/Ni}Y_2)} - \Delta\rho_{(\text{TMD})} - \Delta\rho_{(\text{Ni}Y_2)}, \qquad (1)$$

where $\Delta\rho_{(\text{TMD/Ni}Y_2)}$, $\Delta\rho_{(\text{TMD})}$, and $\Delta\rho_{(\text{Ni}Y_2)}$ represent the charge density of the TMD/NiY_2 heterostructure, of the isolated monolayer TMD, and of the NiY_2, respectively. The plane-averaged charge-density difference $\Delta\rho(z)$ along the z direction is obtained from

$$\Delta\rho(z) = \frac{1}{A_{xy}} \int \Delta\rho \, dx \, dy, \qquad (2)$$

where A_{xy} is the surface area of the unit cell. As charge transfer between adjacent layers is very hard in the semiconductive type-I and type-II heterostructures, there is a much smaller interlayer charge transfer and interfacial charge redistribution than in the conductive type-III heterostructures. For the $WTe_2/NiCl_2$ and $MoTe_2/NiBr_2$ bilayers, the plane-averaged charge density difference is such that $\Delta\rho(z) > 0$ near the interfacial Cl (Br) atoms, and $\Delta\rho(z) < 0$ near the interfacial Te atoms, which means that charge accumulates near the $NiCl(Br)_2$ layer but reduces near the W(Mo)Te_2 layer, while the MoS_2/NiI_2 bilayer shows the opposite situation; see Figs. 3(a)–3(c). Our Bader charge analysis [53,54] also shows that there is a small amount of electron transfer (approximately $0.03e^-$) from the WTe_2 layer to the $NiCl_2$ layer within a 1×1 unit cell, but nearly no charger transfer occurs in the MoS_2/NiI_2 and $NiBr_2/MoTe_2$ heterobilayers. This is due to the fact that Cl is more electronegative than Te, and so it tends to gain electrons from Te, and the characteristics of the type-III band alignment make charger transfer easy.

Because the occupying electrons of the WTe_2 transfer to the $NiCl_2$, holes are created in the WTe_2 layer, just as in the case of p-type doping. It is found that an out-of-plane magnetic moment of 0.01 μ_B is induced in the W atoms in the type-III $WTe_2/NiCl_2$ heterobilayer; however, nearly zero magnetic moment is induced in the Mo and W atoms in the type-I MoS_2/NiI_2 and type-II $MoTe_2/NiBr_2$ heterobilayers. The induced magnetic moment in the WTe_2 layer allows a magnetic coupling with the $NiCl_2$ layer that greatly enhance the splitting. However, for type-I and type-II vdW heterostructures, due to the lack of charge transfer, the exchange interaction is negligible. In this case, the valley degeneracy is lifted only by the breaking of time-reversal symmetry by the magnetic substrate, and so only a small valley splitting can be achieved. We note that the charge transfer in these vdW heterostructures is a kind of spatial transfer rather than a chemical-bond transfer, and so the induced magnetic moment in the Mo and W atoms is very small. Such situations are different from the case of a $MoTe_2$/EuO heterostructure [20,21], where a large charge transfer occurs and a modest magnetic moment (approximately 0.43 μ_B) is induced in the Mo atoms, and so the giant total valley splitting obtained (approximately 44 meV) is due to the strong magnetic coupling that is effective between adjacent layers.

Though the charge transfer in type-III vdW heterostructures is weak, its presence or absence plays a crucial role in the size of the valley splitting. The existence of charge transfer gives rise to hybridization and stronger Coulomb interactions between the monolayer TMD and the NiY_2 layer that greatly enhance the valley splitting. As we can see from the orbital-projected band structures of the $WTe_2/NiCl_2$ bilayer in Fig. 3(d), there are p-d and d-d couplings between the WTe_2 and $NiCl_2$ layers. In the K valley, the spin-polarized states of the two degenerate conduction bands (CBs) of $NiCl_2$ are spin-down, consisting of Ni d^-_{xy,x^2-y^2} and Ni $d^-_{xz,yz}$, and the states of the two valence bands (VBs) of WTe_2 consist of W d^+_{xy,x^2-y^2} and

Te $p^{\pm}_{x,y}$, where the VBM (VB1) is spin-down, but VBM+1 (VB2) is spin-up. VB1 of WTe_2 and the CB of $NiCl_2$ have the same spin-polarized states, and strong hybridization is allowed between them. For the p-d coupling, the Te $d^{-}_{x,y}$ orbital experiences coupling with Ni d^{-}_{xy,x^2-y^2}; the CB of $NiCl_2$ is an antibonding state, and its energy is pushed up. The VBM of WTe_2 is a bonding states, and its energy is pushed down. The d-d coupling is the same as the p-d coupling, and the vast majority of it is W d^{-}_{xy,x^2-y^2} coupled with Ni $d^{-}_{xz,yz}$. Since the SOC is included, an anisotropic d-d coupling between W d^{-}_{xy,x^2-y^2} and Ni $d^{-}_{xz,yz}$ is also allowed, but the coupling intensity is much weaker than that of the isotropic coupling; it almost does not change the energy. However, VB2 of WTe_2 and the CB of $NiCl_2$ have opposite spin-polarized states, and then p-d coupling is forbidden, and the energy of VB2 of WTe_2 does not change (see Fig. S3 in the Supplemental Material [50]). Therefore, the valence-band splitting in WTe_2 in the K valley suffers a decrease because of the effect of hybridization, which results from an energy decrease of VB1. As Δ_{VB} is the energy difference in VB1 between K and K', the energy decrease of VB1 in the K valley is in fact also the size of the valley splitting of the WTe_2. This is because in the K' valley, VB1 of WTe_2 is spin-up and has opposite spin states to the CB of $NiCl_2$. Then p-d coupling is forbidden, and the anisotropic d-d coupling is too weak to shift the energy level, and so the valence-band splitting in WTe_2 at K' does not undergo any change.

The Coulomb interaction also affects the valley splitting, and the size of the splitting is positively correlated with it. In the K valley, VB1 of WTe_2 is repelled downward to VB2 by the Coulomb repulsion; such a reduction in energy is also one of the sources of valley splitting. The existence of a larger charger transfer in type-III vdW

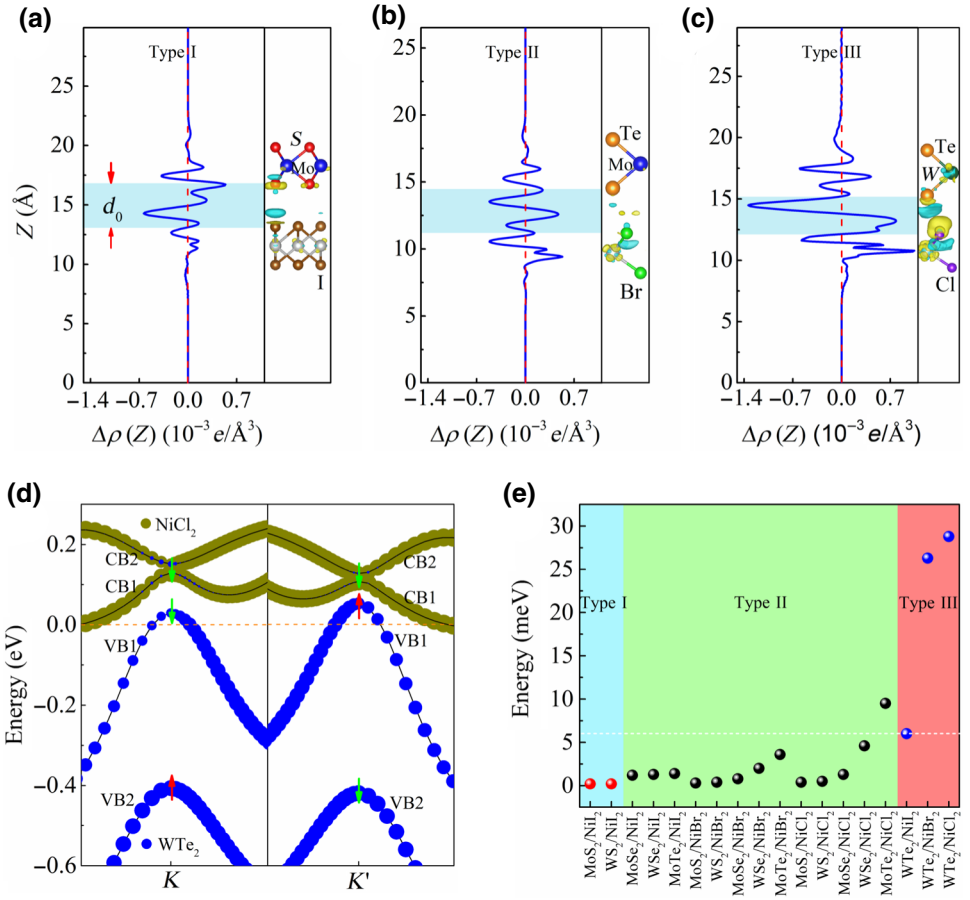

FIG. 3. Interfacial charge transfer in vdW heterostructures with three types of band alignment. (a)–(c) Plane-averaged charge-density difference $\Delta\rho(z)$ along the z direction (left), and side view of plots of the three-dimensional charge-density difference (right) in type-I MoS_2/NiI_2, type-II $MoTe_2/NiBr_2$, and type-III $WTe_2/NiCl_2$ heterobilayers. The isovalue chosen to plot the isosurfaces is 0.0002 eÅ^{-3}. Losses and gains of electrons are colored yellow and aqua, respectively. (d) Orbital-projected band structures of the $WTe_2/NiCl_2$ heterobilayer near the K and K' valleys. The contributions from WTe_2 are the W $d_{xy}+d_{x^2-y^2}$ and Te p_x+p_y orbitals, and those from $NiCl_2$ are Ni d_{xy,x^2-y^2} and Ni $d_{xz,yz}$. The sizes of the symbols are proportional to their population in the corresponding state. Red and green arrows represent spin-up and spin-down states, respectively. (e) Comparison of the largest size of valence valley splitting in monolayer TMDs for the three types of vdW heterostructure.

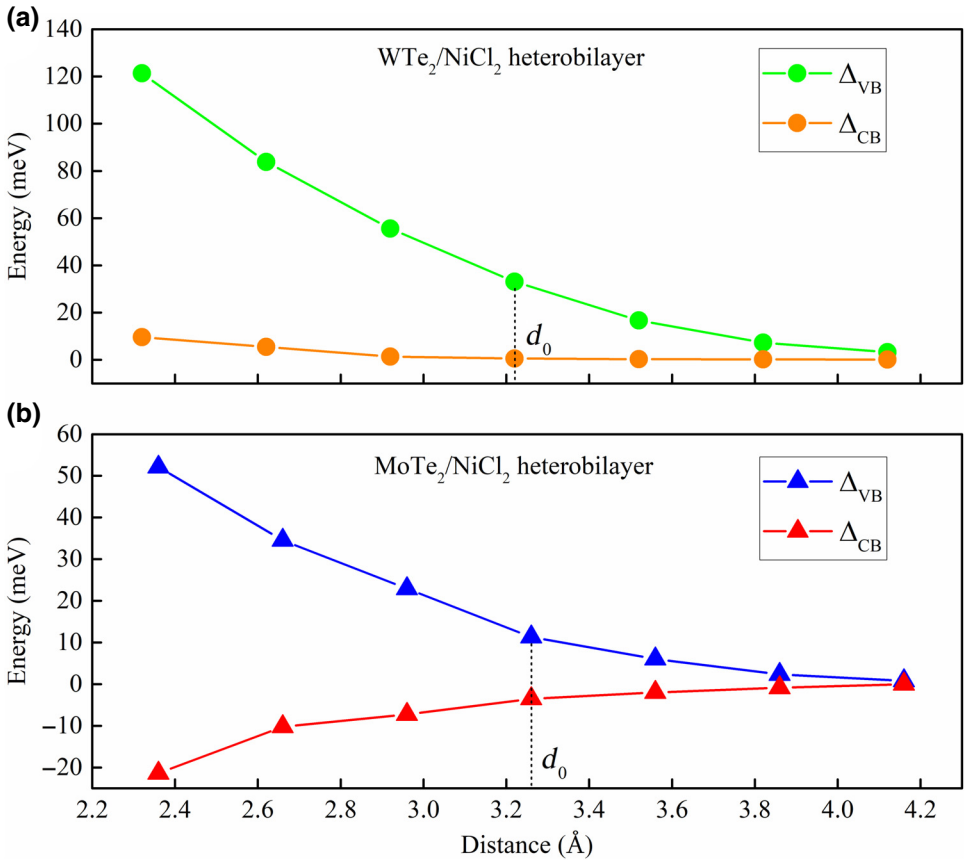

FIG. 4. Valley-splitting changes versus interlayer distance in (a) a $WTe_2/NiBr_2$ heterobilayer, and (b) a $MoTe_2/NiBr_2$ heterobilayer. Δ_{VB} and Δ_{CB} represent the valence and conduction valley splittings, respectively. The equilibrium distance d_0 is denoted by the dashed line.

heterostructures reduces the equilibrium distance d_0 and also reduces $d_{W\text{-}Ni}$ and $d_{Te\text{-}Ni}$; see Figs. 3(a)–3(c). This not only provides a stronger Coulomb field, which enhances the Coulomb repulsion and thereby enhances the valley splitting [55], but also enhances the magnetic proximity effect of the W and Ni atoms, which further enlarges the valley splitting. Moreover, it can be seen that when the TMD is changed from MoS_2 to WTe_2, the energy of the VBM is increased, making the energy difference from the CBM of NiY_2 decrease [Fig. 1(a)]. Then, the Coulomb repulsion between the CBM of NiY_2 and the VBM of the TMD becomes stronger, leading to a reduction of the energy of the valence band and an increase in the splitting in the TMD. As a result, Δ_{VB} in one type of TMD/NiY_2 heterobilayer increases when the TMD is changed from MoS_2 to WTe_2, see Fig. 3(e). The energy differences between the VBM of the TMD and the CB of the NiY_2 at K or K' generally have smaller values in type-III heterostructures, indicating that there exists a stronger intrinsic Coulomb interaction, which helps to produce a relatively larger splitting.

Figure 3(e) also compares the sizes of the valence valley splitting in monolayer TMDs achieved with different types of band alignment in vdW heterostructures. Clearly, the size of the splitting in type-I and type-II heterostructures is indeed much smaller than that in type-III heterostructures, and is typically an order of magnitude smaller than the latter. This is because all of the type-I and type-II heterostructures are semiconductors [33], and the valley degeneracy is lifted only by the magnetism of the ferromagnetic substrate, very like the case of exposing a TMD to an external magnetic field. However, in addition to the situation in the former case, the existence of charge transfer in type-III heterostructures leads to the TMD gaining or losing electron as in the case of p-type or n-type doping. This not only causes finite intrinsic magnetic moments induced in the TMD to allow magnetic coupling with the magnetic material, but also produces a stronger Coulomb field that greatly enhances the valley splitting. Additionally, we note that the splitting in the type-III WTe_2/NiI_2 bilayer is smaller than that in the type-II $MoTe_2/NiCl_2$ bilayer, mainly because the former is constructed from a supercell, where the average W-Ni atom superposition ratio is much smaller, eventually leading to a relatively small splitting.

According to the above analysis, we know that the effect of stacking on valley splitting actually occurs by changing the magnetic coupling between magnetic-metal and transition-metal atoms. Such an effect is the same for all types of heterostructure, and it does not change the rule that for the same stacking, type-III heterostructures have a larger splitting than type-I and type-II heterostructures. This indicates a simple method for seeking a large valley splitting in TMD/2D-magnetic-material vdW

heterostructures, i.e., to select those magnetic materials which can form a type-III band alignment with the monolayer TMD. Also, to further increase the magnitude of the valley splitting, stacking the heterostructure configuration with more superpositions of magnetic-metal and transition-metal atoms is essential.

D. Vertical-stress regulation

The valley splitting is associated with the magnetic coupling effect between the Mo or W and Ni atoms and the Coulomb interaction between adjacent layers, which is closely related to the interlayer distance, and so it is natural to adjust the valley splitting by vertical-stress regulation. In Fig. 4, we adjust the C-2-stacked $WTe_2/NiCl_2$ and $MoTe_2/NiCl_2$ bilayers by vertical stress. It can be seen that the size of the valley splitting is negatively correlated with the interlayer spacing. When d_0 is decreased, the Coulomb field between adjacent layers is enhanced, and the decreased interatomic distance between Mo or W and Ni enhances the coupling between Mo or W and Ni atoms. As a result, the valley splitting is increased. In the type-III $WTe_2/NiCl_2$ bilayer, a total splitting of more than 112 meV can be obtained by reducing the interlayer distance, corresponding to an equivalent magnetic field of 560 T. More interestingly, a total splitting of over 73.5 meV can be achieved in the type-II $MoTe_2/NiCl_2$ bilayer by this form of regulation, and the characteristics of the type-II band alignment of the heterobilayer and the direct band gap of the monolayer $MoTe_2$ remain unchanged. For the $WTe_2/NiCl_2$ bilayer, the K valley is shifted below the Fermi level (see Fig. S4 in the Supplemental Material [50]). These band variations make it easier to collect electron-hole pairs by optical means. In contrast, when d_0 is increased, the charger transfer between adjacent layers becomes more difficult, which weakens both the Coulomb field and the coupling between Mo or W and Ni atoms, so that Δ_{VB} and Δ_{CB} are reduced. When d_0 is increased to 4.20 Å, the splitting becomes zero, which means that the magnetic-proximity coupling in the heterobilayer is a short-range effect. Owing to the giant valley splitting in TMD/NiY_2 vdW heterostructures, one can selectively excite valley-dependent electron-hole pairs with circularly polarized light over a rather wide spectral range. In experiments, the interlayer distance can be adjusted by applying an external perpendicular pressure [56,57], and so these results could greatly advance the development of valley electronics.

IV. CONCLUSION

In summary, a comparative study is performed on a series of TMD/2D-magnetic-material vdW heterostructures to investigate the rules governing valley splitting. The monolayer NiY_2 semiconductors possess out-of-plane magnetism and have a matched momentum space with TMDs, which makes them potentially excellent magnetic substrates. In the type-III $WTe_2/NiCl_2$ heterobilayer, the largest total valley splitting reaches 32.5 meV at the equilibrium interlayer distance, and can even reach 112 meV with vertical-stress regulation. This will make it easier to excite valley-dependent electron-hole pairs by optical means. It is found that the same order of magnitude of splitting can be achieved in most of the type-III heterostructures, while the largest sizes in all type-I and type-II heterostructures are typically only several millielectronvolts, an order of magnitude smaller than the former values. This is because there is enough charge transfer between the TDM and the magnetic substrate in type-III heterostructures to enhance the magnetic coupling and Coulomb interaction, which greatly enhances the valley splitting, while that does not happen in type-I and type-II heterostructures. Moreover, the adjustment of the valley splitting by means of the stacking actually occurs by regulating the strength of the magnetic coupling between the magnetic-metal and transition-metal atoms, which is closely related to the interatomic distance and atomic superposition. Although the stacking can vary the valley splitting to a large extent, this effect is the same for all types of heterostructure. It does not change the rule that for the same stacking, the type-III heterostructures typically possess a larger valley splitting. These findings give ideas about how to seek and design large valley splittings in type-III vdW heterostructures, and these predicted heterostructures will provide new and excellent experimental candidates for valleytronics research and may even advance the application of quantum-information devices.

ACKNOWLEDGMENTS

This work is supported by the National Natural Science Foundation of China through Grants No. 11674090 and No. 11347022, and by the Hunan Provincial Natural Science Foundation of China (Grant No. 2019JJ40029). The computational resources are provided by the TianHe supercomputer in Changsha, China.

[1] D. Xiao, M.-C. Chang, and Q. Niu, Berry phase effects on electronic properties, Rev. Mod. Phys. **82**, 1959 (2010).
[2] J. R. Schaibley, H. Yu, G. Clark, P. Rivera, J. S. Ross, K. L. Seyler, W. Yao, and X. Xu, Valleytronics in 2D materials, Nat. Rev. Mater. **1**, 16055 (2016).
[3] Y. S. Ang, S. A. Yang, C. Zhang, Z. Ma, and L. K. Ang, Valleytronics in merging Dirac cones: All-electric-controlled valley filter, valve, and universal reversible logic gate, Phys. Rev. B **96**, 245410 (2017).
[4] G.-B. Liu, D. Xiao, Y. Yao, X. Xu, and W. Yao, Electronic structures and theoretical modelling of two-dimensional group-VIB transition metal dichalcogenides, Chem. Soc. Rev. **44**, 2643 (2015).

[5] X. Xu, W. Yao, D. Xiao, and T. F. Heinz, Spin and pseudospins in layered transition metal dichalcogenides, Nat. Phys. **10**, 343 (2014).

[6] W. Feng, Y. Yao, W. Zhu, J. Zhou, W. Yao, and D. Xiao, Intrinsic spin Hall effect in monolayers of group-VI dichalcogenides:A first-principles study, Phys. Rev. B **86**, 165108 (2012).

[7] K. F. Mak, K. L. McGill, J. Park, and P. L. McEuen, The valley Hall effect in MoS_2 transistors, Science **344**, 1489 (2014).

[8] A. M. Jones, H. Y. Yu, N. J. Ghimire, S. F. Wu, G. Aivazian, J. S. Ross, B. Zhao, J. Q Yan, D. G. Mandrus, D. Xiao, W. Yao, and X. Xu, Optical generation of excitonic valley coherence in monolayer WSe_2, Nat. Nanotechnol. **8**, 634 (2013).

[9] K. F. Mak, K. L. He, J. Shan, and T. F. Heinz, Control of valley polarization in monolayer MoS_2 by optical helicity, Nat. Nanotechnol. **7**, 494 (2012).

[10] T. Cao, G. Wang, W. Han, H. Ye, C. Zhu, J. Shi, Q. Niu, P. Tan, E. Wang, B. Liu, and J. Feng, Valley-selective circular dichroism of monolayer molybdenum disulphide, Nat. Commun. **3**, 887 (2012).

[11] H. Zeng, J. Dai, W. Yao, D. Xiao, and X. Cui, Valley polarization in MoS_2 monolayers by optical pumping, Nat. Nanotechnol. **7**, 490 (2012).

[12] M. Manca, M. M. Glazov, C. Robert, F. Cadiz, T. Taniguchi, K. Watanabe, E. Courtade, T. Amand, P. Renucci, X. Marie, G. Wang, and B. Urbaszek, Enabling valley selective exciton scattering in monolayer WSe_2 through upconversion, Nat. Commun. **8**, 14927 (2017).

[13] J. Lee, K. F. Mak, and J. Shan, Electrical control of the valley Hall effect in bilayer MoS_2 transistors, Nat. Nanotechnol. **11**, 421 (2016).

[14] S. Wu, J. S. Ross, G.-B. Liu, G. Aivazian, A. Jones, Z. Fei, W. Zhu, D. Xiao, W. Yao, D. Cobden, and X. Xu, Electrical tuning of valley magnetic moment through symmetry control in bilayer MoS_2, Nat. Phys. **9**, 149 (2013).

[15] G. Aivazian, Z. Gong, A. M. Jones, R.-L. Chu, J. Yan, D. G. Mandrus, C. Zhang, D. Cobden, W. Yao, and X. Xu, Magnetic control of valley pseudospin in monolayer WSe_2, Nat. Phys. **11**, 148 (2015).

[16] D. MacNeill, C. Heikes, K. F. Mak, Z. Anderson, A. Kormányos, V. Zólyomi, J. Park, and D. C. Ralph, Breaking of Valley Degeneracy by Magnetic Field in Monolayer $MoSe_2$, Phys. Rev. Lett. **114**, 037401 (2015).

[17] Y. Cheng, Q. Zhang, and U. Schwingenschlögl, Valley polarization in magnetically doped single-layer transition-metal dichalcogenides, Phys. Rev. B **89**, 155429 (2014).

[18] N. Singh and U. Schwingenschlögl, A route to permanent valley polarization in monolayer MoS_2, Adv. Mater. **29**, 1600970 (2017).

[19] S. Q. Guo, Y. Y. Wang, C. Wang, Z. L. Tang, and J. Y. Zhang, Large spin-orbit splitting in the conduction band of halogen (F, Cl, Br, and I) doped monolayer WS_2 with spin-orbit coupling, Phys. Rev. B **96**, 245305 (2017).

[20] J. Qi, X. Li, Q. Niu, and J. Feng, Giant and tunable valley degeneracy splitting in $MoTe_2$, Phys. Rev. B **92**, 121403(R) (2015).

[21] Q. Zhang, S. A. Yang, W. Mi, Y. Cheng, and U. Schwingenschlögl, Large spin-valley polarization in monolayer $MoTe_2$ on top of EuO(111), Adv. Mater. **28**, 959 (2016).

[22] C. Zhao, T. Norden, P. Zhang, P. Zhao, Y. Cheng, F. Sun, J. P. Parry, P. Taheri, J. Wang, Y. Yang, T. Scrace, K. Kang, S. Yang, G.-X. Miao, R. Sabirianov, G. Kioseoglou, W. Huang, A. Petrou, and H. Zeng, Enhanced valley splitting in monolayer WSe_2 due to magnetic exchange field, Nat. Nanotechnol. **12**, 757 (2017).

[23] L. Xu, M. Yang, L. Shen, J. Zhou, T. Zhu, and Y. P. Feng, Large valley splitting in monolayer WS_2 by proximity coupling to an insulating antiferromagnetic substrate, Phys. Rev. B **97**, 041405(R) (2018).

[24] D. Zhong, K. L. Seyler, X. Linpeng, R. Cheng, N. Sivadas, B. Huang, E. Schmidgall, T. Taniguchi, K. Watanabe, M. A. McGuire, W. Yao, D. Xiao, K.-M. C. Fu, and X. Xu, Van der Waals engineering of ferromagnetic semiconductor heterostructures for spin and valleytronics, Sci. Adv. **3**, e1603113 (2017).

[25] K. Zhang, L. Wang, and X. Wu, Spin polarization and tunable valley degeneracy in a MoS_2 monolayer via proximity coupling to a Cr_2O_3 substrate, Nanoscale **11**, 19536 (2019).

[26] T. Norden, C. Zhao, P. Y. Zhang, R. Sabirianov, A. Petrou, and H. Zeng, Giant valley splitting in monolayer WS_2 by magnetic proximity effect, Nat. Commun. **10**, 4163 (2019).

[27] B. Huang, G. Clark, E. Navarro-Moratalla, D. R. Klein, R. Cheng, K. L. Seyler, D. Zhong, E. Schmidgall, M. A. McGuire, D. H. Cobden, W. Yao, D. Xiao, P. Jarillo-Herrero, and X. Xu, Layer-dependent ferromagnetism in a van der Waals crystal down to the monolayer limit, Nature **546**, 270 (2017).

[28] N. Mounet, M. Gibertini, P. Schwaller, D. Campi, A. Merkys, A. Marrazzo, T. Sohier, I. E. Castelli, A. Cepellotti, G. Pizzi, and N. Marzari, Two-dimensional materials from high-throughput computational exfoliation of experimentally known compounds, Nat. Nanotechnol. **13**, 246 (2018).

[29] K. S. Novoselov, A. Mishchenko, A. Carvalho, A. H. Castro Neto, and O. Road, 2D materials and van der Waals heterostructures, Science **353**, aac9439 (2016).

[30] Q. Z. Li, L. P. Tang, C. X. Zhang, D. Wang, Q.-J. Chen, Y.-X. Feng, L.-M. Tang, and K.-Q. Chen, Seeking the Dirac cones in the MoS_2/WSe_2 van der Waals heterostructure, Appl. Phys. Lett. **111**, 171602 (2017).

[31] K. L. Seyler, D. Zhong, B. Huang, X. Linpeng, N. P.Wilson, T. Taniguchi, K. Watanabe, W. Yao, D. Xiao, M. A. McGuire, K.-M. C. Fu, and X. Xu, Valley manipulation by optically tuning the magnetic proximity effect in WSe_2/CrI_3 heterostructures, Nano Lett. **18**, 3823 (2018).

[32] Z. Zhang, X. J. Ni, H. Q. Huang, L. Hu, and F. Liu, Valley splitting in the van der Waals heterostructure WSe_2/CrI_3: The role of atom superposition, Phys. Rev. B **99**, 115441 (2019).

[33] V. O. Özçelik, J. G. Azadani, C. Yang, S. J. Koester, and T. Low, Band alignment of two-dimensional semiconductors for designing heterostructures with momentum space matching, Phys. Rev. B **94**, 035125 (2016).

[34] J. P. Perdew, K. Burke, and M. Ernzerhof, Generalized Gradient Approximation Made Simple, Phys. Rev. Lett. **77**, 3865 (1996).

[35] G. Kresse and J. Furthmüller, Efficient iterative schemes for ab initio total-energy calculations using a plane-wave basis set, Phys. Rev. B **54**, 11169 (1996).
[36] P. E. Blöchl, Projector augmented-wave method, Phys. Rev. B **50**, 17953 (1994).
[37] S. Grimme, Semiempirical GGA-type density functional constructed with a long-range dispersion correction, J. Comput. Chem. **27**, 1787 (2006).
[38] I. V. Solovyev, P. H. Dederichs, and V. I. Anisimov, Corrected atomic limit in the local-density approximation and the electronic structure ofdimpurities in Rb, Phys. Rev. B **50**, 16861 (1994).
[39] F. Tran, J. Stelzl, and P. Blaha, Rungs 1 to 4 of DFT Jacob's ladder: Extensive test on the lattice constant, bulk modulus, and cohesive energy of solids, J. Chem. Phys. **144**, 204120 (2016).
[40] V. V. Kulish and W. Huang, Single-layer metal halides MX_2 ($X = \mathrm{Cl, Br, I}$): Stability and tunable magnetism from first principles and Monte Carlo simulations, J. Mater. Chem. C **5**, 8734 (2017).
[41] A. A. Mostofi, J. R. Yates, Y.-S. Lee, I. Souza, D. Vanderbilt, N. Marzari, wannier90: A tool for obtaining maximally-localised Wannier functions, Comput. Phys. Commun. **178**, 685 (2008).
[42] N. Marzari, A. A. Mostofi, J. R. Yates, I. Souza, and D. Vanderbilt, Maximally localized Wannier functions: Theory and applications, Rev. Mod. Phys. **84**, 1419 (2012).
[43] T. Kurumaji, S. Seki, S. Ishiwata, H. Murakawa, Y. Kaneko, and Y. Tokura, Magnetoelectric responses induced by domain rearrangement and spin structural change in triangular-lattice helimagnets NiI_2 and CoI_2, Phys. Rev. B **87**, 014429 (2013).
[44] Z. Jiang, P. Wang, J. P. Xing, X. Jiang, and J. J. Zhao, Screening and design of novel 2D ferromagnetic materials with high curie temperature above room temperature, ACS Appl. Mater. Interfaces **10**, 39032 (2018).
[45] K. F. Mak, C. Lee, J. Hone, J. Shan, T. F. Heinz, Atomically Thin MoS_2: A New Direct-Gap Semiconductor, Phys. Rev. Lett. **105**, 136805 (2010).
[46] A. Togo, L. Chaput, and I. Tanaka, Distributions of phonon lifetimes in Brillouin zones, Phys. Rev. B **91**, 094306 (2015).
[47] G. F. Xie, D. Ding, and G. Zhang, Phonon coherence and its effect on thermal conductivity of nanostructures, Adv. Phys.: X **3**, 1480417 (2018).
[48] L. P. Tang, L.-M. Tang, D. Wang, H.-X. Deng, and K.-Q. Chen, Metal and ligand effects on the stability and electronic properties of crystalline twodimensional metal-benzenehexathiolate coordination compound, J. Phys.: Condens. Matter **30**, 465301 (2018).
[49] L. P. Tang, Q. Z. Li, C. X. Zhang, F. Ning, W.-X. Zhou, L.-M. Tang, and K.-Q Chen, Prediction of intrinsic ferromagnetism in two-dimension planar metalorganic framework semiconductors, J. Magn. Magn. Mater. **488**, 165354 (2019).
[50] See the Supplemental Material for http://link.aps.org/supplemental/10.1103/PhysRevApplied.13.014064 a stability analysis and band structures of the TMD/NiY_2 heterobilayers, the orbital-projected band structure of $WTe_2/NiCl_2$ heterobilayers, and the valley splitting under vertical-stress regulation.
[51] N. Cortés, O. Ávalos-Ovando, L. Rosales, P. A. Orellana, and S. E. Ulloa, Tunable Spin-Polarized Edge Currents in Proximitized Transition Metal Dichalcogenides, Phys. Rev. Lett. **122**, 086401 (2019).
[52] G.-B. Liu, W.-Y. Shan, Y. Yao, W. Yao, and D. Xiao, Three-band tight-binding model for monolayers of group-VIB transition metal dichalcogenides, Phys. Rev. B **88**, 085433 (2013).
[53] G. Henkelman, A. Arnaldsson, and H. Jónsson, A fast and robust algorithm for Bader decomposition of charge density, Comput. Mater. Sci. **36**, 354 (2006).
[54] D. Wang, L.-M. Tang, X. X. Jiang, J. Y. Tan, M.-D. He, X-Jun Wang, and K.-Q. Chen, High bipolar conductivity and robust in-plane spontaneous electric polarization in selenene, Adv. Electron. Mater. **5**, 1800475 (2019).
[55] H.-X. Deng, J.-W. Luo, S.-S. Li, and S.-H. Wei, Origin of the Distinct Diffusion Behaviors of Cu and Ag in Covalent and Ionic Semiconductors, Phys. Rev. Lett. **117**, 165901 (2016).
[56] A. P. Nayak, S. Bhattacharyya, J. Zhu, J. Liu, X. Wu, T. Pandey, C. Jin, A. K. Singh, D. Akinwande, and J.-F. Lin, Pressure-induced semiconducting to metallic transition in multilayered molybdenum disulphide, Nat. Commun. **5**, 3731 (2014).
[57] Z. Zhao, H. Zhang, H. Yuan, S. Wang, Y. Lin, Q. Zeng, G. Xu, Z. Liu, G. Solanki, K. Patel, Y. Cui, H. Hwang, and W. L. Mao, Pressure induced metallization with absence of structural transition in layered molybdenum diselenide, Nat. Commun. **6**, 7312 (2015).